Improved Coastal Precipitation Forecasts with Direct Assimilation of *GOES-11/12* Imager Radiances

XIAOLEI ZOU

Department of Earth, Ocean, and Atmospheric Sciences, The Florida State University, Tallahassee, Florida

ZHENGKUN QIN

Department of Earth, Ocean, and Atmospheric Sciences, The Florida State University, Tallahassee, Florida, and Center of Data Assimilation for Research and Application, Nanjing University of Information and Science and Technology, Nanjing, China

FUZHONG WENG

National Environmental Satellite, Data, and Information Service, National Oceanic and Atmospheric Administration, Washington, D.C.

(Manuscript received 22 October 2010, in final form 30 May 2011)

ABSTRACT

The Geostationary Operational Environmental Satellite (GOES) imager provides observations that are of high spatial and temporal resolution and can be applied for effectively monitoring and nowcasting severe weather events. In this study, improved quantitative precipitation forecasts (QPFs) for three coastal storms over the northern Gulf of Mexico and the East Coast is demonstrated by assimilating *GOES-11* and *GOES-12* imager radiances into the Weather Research and Forecasting (WRF) model. Both the National Centers for Environmental Prediction (NCEP) Gridpoint Statistical Interpolation (GSI) analysis system and the Community Radiative Transfer Model (CRTM) are utilized to ingest GOES IR clear-sky data. Assimilation of GOES imager radiances during a 6–12-h time window prior to convective initiation and/or development could significantly improve the precipitation forecasts near the coast of the northern Gulf of Mexico. The 3-h accumulative precipitation threat scores are increased by about 20% after 6 h of model forecasts and more than 50% after 18–24 h of model forecasts. A detailed diagnosis of analysis fields and model forecast fields is carried out for one of the three convective precipitation events included in this study. It is shown that the assimilation of GOES data in regions of no or little clouds improved the model description of an upstream midlatitude trough and a subtropical high located in the south of the convection. The GOES observations located in the western part of land region covered by GOES within the latitude zone of 18°–37°N near 100°W contributed to a better forecast of the position of the eastward-propagating trough, while GOES observations over the Gulf of Mexico increased the amount of water vapor advection from the south into the convective region by the wind associated with the subtropical high. In the past, GOES imager radiances were not directly used in the GSI system. This study highlights the importance of satellite imagery information observed in the preconvective environment for improved cloud and precipitation forecasts. The developed data assimilation technique will prepare the NWP user community for accelerated use of advanced satellite data from the GOES-R series.

1. Introduction

It is well known nowadays that satellite observations are indispensable in numerical weather prediction (NWP) systems. The development of fast radiative transfer models has (McMillin and Fleming 1976; Saunders et al. 1999, 2007; Weng 2007) has allowed for the direct assimilation of satellite infrared and microwave radiances, instead of satellite retrieval products, in NWP systems. Significant improvements have been made in NWP forecast skill by meteorological satellites, mostly as a result of polar-orbiting systems that been developed recently (Eyre et al. 1993; Andersson et al. 1994).

More recently, efforts have been made to introduce radiance observations from geostationary satellites into

Corresponding author address: Xiaolei Zou, Dept. of Earth, Ocean, and Atmospheric Sciences, The Florida State University, 404 Love Bldg., Tallahassee, FL 32306-4520.
E-mail: xzou@fsu.edu

DOI: 10.1175/MWR-D-10-05040.1

© 2011 American Meteorological Society

TABLE 1. Experiment design for 24-h precipitation forecasts during 0000–2400 UTC 23 May 2008. DA: direct assimilation.

	22 May 2008			23 May 2008
Time (UTC)	0600	1200	1800	0000–2400
CTRL1	$\mathbf{x}_b$	36-h forecast		
CTRL2				
CONV	$\mathbf{x}_b$	DA for conventional data		24-h forecast
SATCONV	$\mathbf{x}_b$	DA for GOES imager data and conventional data		

TABLE 2. Experiment design for 27-h precipitation forecasts from 1800 UTC 20 Jun to 2100 UTC 21 Jun 2008.

	20 Jun 2008			21 Jun 2008
Time (UTC)	0600	1200	1800	0000–2100
CTRL1	$\mathbf{x}_b$	33-h forecast		
CTRL2				
CONV	$\mathbf{x}_b$	DA for conventional data		27-h forecast
SATCONV	$\mathbf{x}_b$	DA for GOES imager data and conventional data		

NWP systems. Although at lower spectral resolution, geostationary instruments provide nearly continuous four-dimensional evolutionary patterns of weather phenomena over the observing domain. Preliminary studies on the assimilation and NWP impacts of the geostationary radiances include Köpken et al. (2004) for the Meteosat Visible and Infrared Imager (MVIRI) on board *Meteosat-7* and Szyndel et al. (2005) and Stengel et al. (2009) for the Spinning Enhanced Visible and Infrared Imager (SEVIRI) on board *Meteosat-8*. The study of Geostationary Operational Environmental Satellite (GOES) imager radiance data in global data assimilations by Su et al. (2003) showed neutral or slightly degraded impacts on the performance of the forecast skill. These studies employed either a global (Köpken et al. 2004; Szyndel et al. 2005) or a regional (Stengel et al. 2009) four-dimensional variational data assimilation (4D-Var) system.

In this paper, we investigate the benefits of directly assimilating GOES radiance data for improving coastal precipitation forecasts. Specifically, imager data from *GOES-11* and *GOES-12* will be assimilated using the National Centers for Environmental Prediction (NCEP) unified Gridpoint Statistical Interpolation (GSI) analysis code (Wu et al. 2002; Purser et al. 2003a,b) to assess their potential impacts on quantitative precipitation forecasts (QPFs) near the coast of the northern Gulf of Mexico.

From GOES high temporal and spatial resolutions, atmospheric motion winds can be derived by tracking the cloud or water-vapor features from infrared channels in sequential satellite images. *GOES-11* and *GOES-12* satellite-derived high-density winds are routinely made available by the Center for Satellite Applications and Research (STAR), at the National Oceanic and Atmospheric Administration/National Environmental Satellite, Data, and Information Service (NOAA/NESDIS; information online at http://www.star.nesdis.noaa.gov/smcd/opdb/goes/winds/wind.html). Details of the infrared cloud-top and water vapor tracking algorithm can be found in Nieman et al. (1993), Velden (1996), and Velden et al. (1997). Many studies have shown some positive impacts on NWP from assimilation of GOES winds (Tomassini et al. 1999; Soden et al. 2001; Goerss et al. 1998; Velden et al. 1998). However, a major shortcoming of assimilating these GOES water-vapor or cloud-tracked winds arises from uncertainty in the height assignment of satellite-derived winds (Rao et al. 2002). This is because the satellites measure radiation emitted from a volume of the atmosphere within the instrument's field of view (FOV) and the GOES-derived cloud-top and water-vapor tracking winds are assigned a specific height. The thickness of the atmospheric volume that contributes to the radiance measurement is described by the so-called weighting function. Therefore, the broader the weighting function is, the larger the errors of the GOES winds are. It is thus advantageous to directly assimilate GOES radiances so that the forward radiative transfer model describes correctly the measured (and assimilated) radiance and the observation errors are simpler.

The NCEP GSI analysis system is a three-dimensional (3D-Var) system. Assimilation of *GOES-11* and *GOES-12* observations in a 3D-Var system with a limited-area model is fairly new and to our knowledge has not yet been evaluated in the peer-reviewed literatures. It is more difficult to assess the benefits of geostationary satellite observations using a regional 3D-Var system than using a global 3D–4D-Var or a regional 4D-Var system for the following reasons: (i) high temporal resolution data features of geostationary satellites cannot yet be fully utilized, (ii) the assimilation cycle and model integration time are usually not longer than 2–3 days due to limited domain

TABLE 3. Experiment design for 18-h precipitation forecasts from 1200 UTC 22 May to 0600 UTC 23 May 2008.

Time (UTC)	22 May 2008				23 May 2008	
	0000	0600	1200	1800	0000	0600
CTRL1	$\mathbf{x}_b$	30-h forecast				
CTRL2						
CONV	$\mathbf{x}_b$	DA for conventional data			18-h forecast	
SATCONV	$\mathbf{x}_b$	DA for GOES imager data and conventional data				

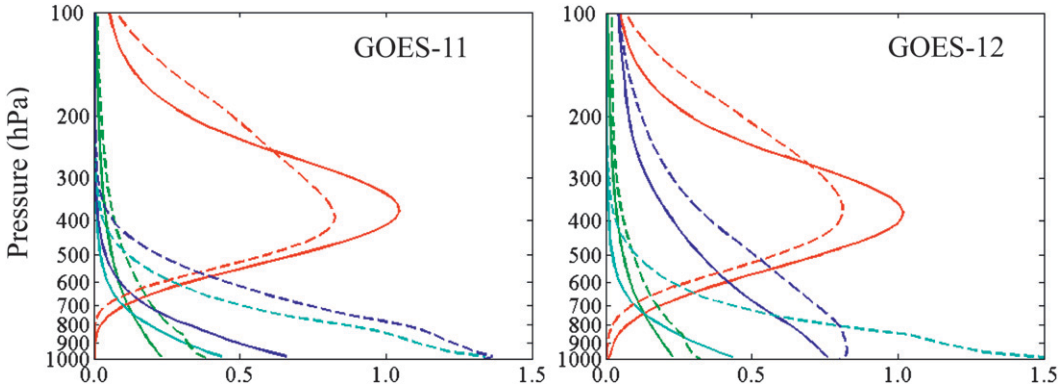

FIG. 1. Weighting functions of GOES imager channels 2 (forest green), 3 (red), 4 (cyan), 5 (*GOES-11*, blue), and 6 (*GOES-12*, blue). Solid lines are calculated from the *U.S. Standard Atmosphere, 1976* profile, and dashed lines are calculated from over 200 and 400 profiles.

sizes, and (iii) the impacts of assimilated satellite data on regional NWP models are constrained by the host model's accuracy at the lateral boundaries. In this study, only the impacts of GOES imager data assimilation on 18–27-h offshore precipitation forecasts are assessed. Since the GOES imager data are thinned in space and assimilated through a 3D-Var system, the high temporal resolution information from the geostationary satellites is probably underutilized in the present study. The assimilation cycle is now limited to no more than 2–3 times, with a 6-h cycling interval, to avoid problems arising from lateral boundary conditions.

This paper is organized as follows. A brief overview of the NCEP GSI system, the *GOES-11/12* data preprocessing, and the data assimilation experiment setup are provided in the following section. The impacts of *GOES-11/12* imager radiances on the NWP analysis fields after assimilation are presented and discussed in section 3. In section 4, forecast errors including coastal precipitation amounts are analyzed with respect to surface observations.

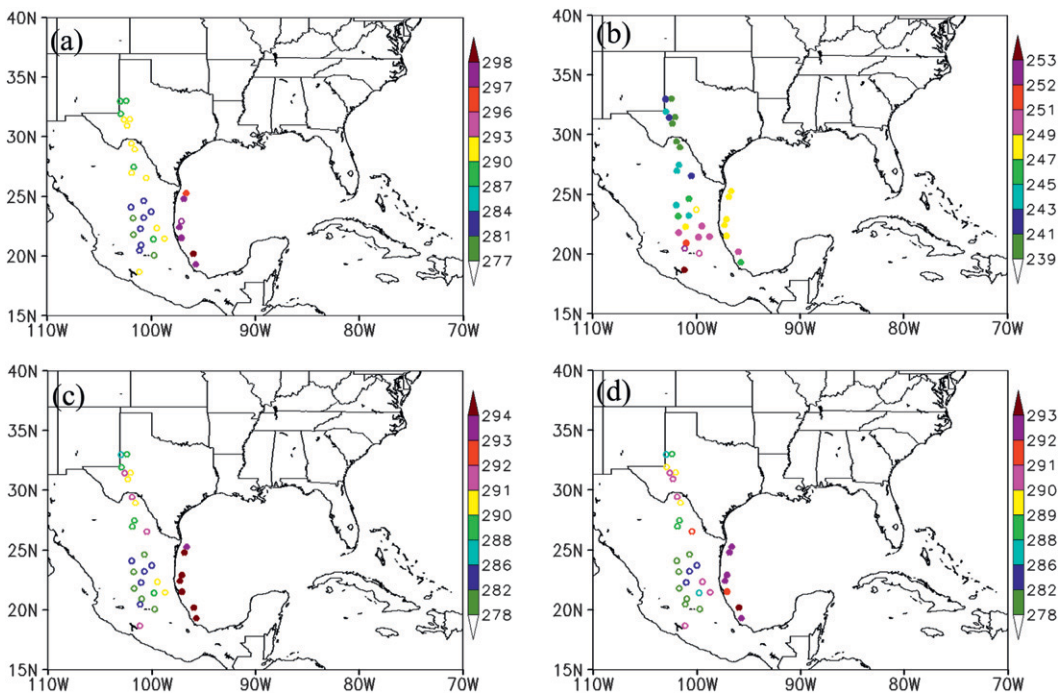

FIG. 2. *GOES-11* observed brightness temperatures (K) from channels (a) 2, (b) 3, (c) 4, and (d) 5 at 1200 UTC 22 May 2008. Observation locations at which the observed radiances did and did not pass the quality control (QC) process are indicated by solid dots and open circles, respectively.

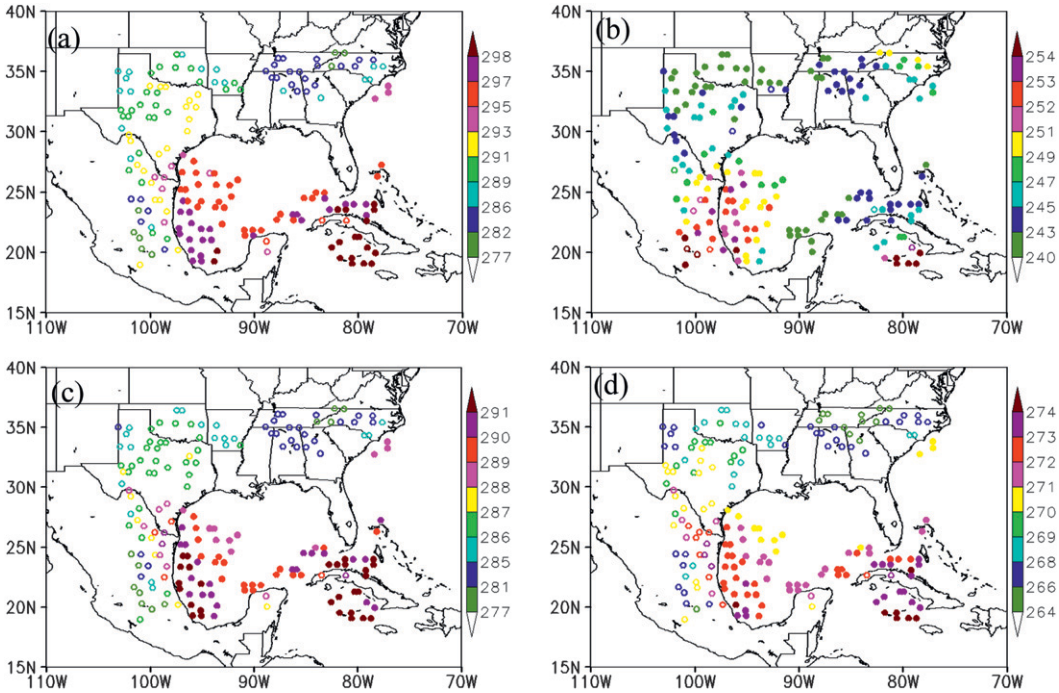

FIG. 3. As in Fig. 2, but for *GOES-12* channels (a) 2, (b) 3, (c) 4, and (d) 6.

2. Methodology

a. The GSI system

The Gridpoint Statistical Interpolation analysis system is a three-dimensional variational data assimilation system for both global and regional applications. It was initially developed as the next-generation global analysis system. An overview of the theory and development of the initial GSI system can be found in Wu et al. (2002). The ability of GSI to adapt more flexibly to large geographical inhomogeneities in the density and quality of the available data is an advantage over the Spectral Statistical Interpolation (SSI) analysis system developed at NCEP (Derber and Wu 1998). By integrating appropriate recursive filters into the analysis system, the spectral definition of background errors in the SSI analysis system is replaced with a gridpoint representation that allows for situation-dependent, anisotropic, and nonhomogenous structures to be built into a background error covariance matrix. Details of the recursive filter techniques can be found in Wu et al. (2002) and Purser et al. (2003a,b). The GSI User's Guide (information online at http://www.dtcenter.org/com-GSI/users/index.php) provides a step-by-step procedure to install, compile, and run the GSI system on different local computer systems. The GSI has been successfully ported to a Linux platform at The Florida State University (FSU), and results in this study are obtained from the FSU local computing facilities.

b. The Community Radiative Transfer Model

The Community Radiative Transfer Model (CRTM) was developed by the U.S. Joint Center for Satellite Data Assimilation (JCSDA) for rapid calculations of satellite radiances and their derivatives under various atmospheric and surface conditions. It was incorporated into the GSI data assimilation system at the NCEP/Environmental Modeling Center (EMC). The CRTM was first released to the public in 2004, and has been substantially improved and expanded since then. It supports a large number of sensors, including the historical and near-future sensors from GOES-R series and the Joint Polar Satellite System (JPSS), covering the microwave, infrared, and visible frequency regions.

The CRTM comprises four major modules for calculations of the (i) atmospheric transmittance, (ii) surface emissivity/reflectivity, (iii) cloud/aerosol optical property, and (iv) radiative transfer solution. In the atmospheric transmittance module, there is a multiple transmittance algorithm framework that allows different transmittance algorithms to coexist. A new transmittance algorithm has recently been implemented that combines the strengths of the Optical Path Transmittance (OPTRAN) and Optical Depth in Pressure Space (ODPS) algorithms that are currently used in the fast Radiative Transfer for the Advanced Television and Infrared Observation Satellite (TIROS) Operational Vertical Sounder (RTTOV) model. The surface emissivity/reflectivity module consists of four

submodules corresponding to ocean, land, snow, and sea ice surfaces. Each of the four submodules consists of smaller modules with their own frequency regions and surface subtypes. An array of physical and empirical surface emissivity and reflectivity models has been implemented into CRTM. For calculations of cloud and aerosol absorption and scattering, lookup tables of the optical properties of six cloud and eight aerosol types are included in the cloud/aerosol optical property module. Finally, the fast doubling–adding method, implemented in the radiative transfer solution module, solves the multistream radiative transfer equation. More details can be found in Weng (2007) and Han et al. (2007).

c. Data

GOES-11 and *-12* satellites are initially positioned in geostationary orbits at 135° and 75°W, respectively, and are part of GOES system operated by NOAA/NESDIS. Orbiting at Earth's rotation speed at an altitude of 35 790-km, both satellites remain stationary with respect to a fixed point on the earth's surface, providing imager data over the West Coast (*GOES-11*, also called *GOES-West*) and East Coast (*GOES-12*, or *GOES-East*) of the United States with an imaging refresh rate of 15 min.

The *GOES-11* imager has one visible and four infrared channels. The central wavelengths for channels 1–5 are 0.65, 3.9, 6.8, 10.7, and 12.0 μm, respectively. The spatial resolutions (i.e., instantaneous geometric field of view) of channels 2, 4, and 5 are 4 km at the subsatellite point, and those of channels 1 and 3 are 1 and 8 km, respectively. Channel 1 is located at a visible wavelength for observing the reflected radiation from the earth and therefore is ideal for detecting the clouds, aerosols, and surface features during daytime. Channel 2 provides the near-infrared radiation for detecting low cloud, fog, and fire. Channel 3 is mainly used for depicting the upper-level water vapor plumes. Channel 4 is for surface and cloud-top temperature, and channel 5 is for low-level water vapor. The *GOES-12* imager also has one visible and four infrared channels. Channels 1, 2, and 4 are the same as *GOES-11*. Comparing with *GOES-11*'s channel 3, the central wavelength of *GOES-12*'s channel 3 is shifted to 6.48 μm and the spatial resolution is increased to 4 km. Channel 5 of *GOES-11* is removed from *GOES-12*. A new CO_2 channel (channel 6) is added to *GOES-12* for cloud detection, with a central wavelength of 13.3 μm and a spatial resolution of 8 km. The new channel is added to improve the height assignment for retrieving cloud-drift winds. An empirical quality control has been applied to all the data before data assimilation; details of quality control can be found in the appendix.

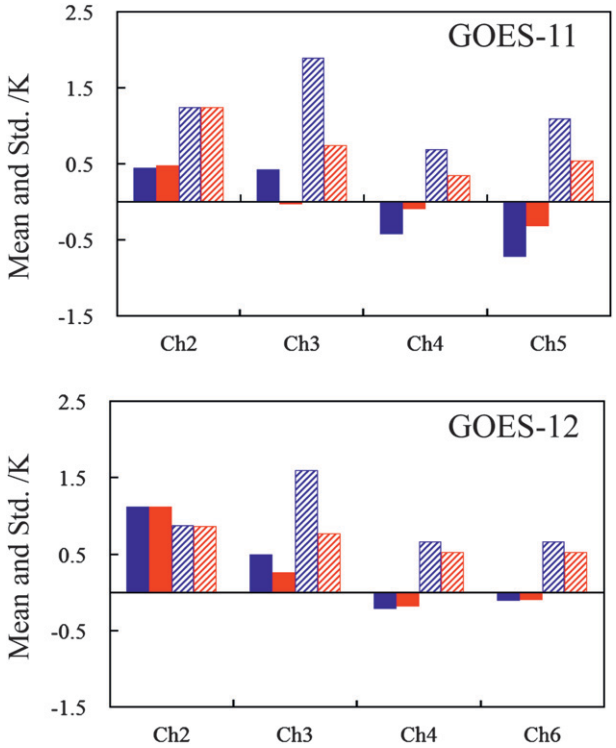

FIG. 4. Biases (solid bars) and RMS errors (dashed bars) of *GOES-11* and *-12* observation departures from the background (blue) and analysis (red) for the SATCONV experiment. Calculations were carried out over a 1-month dataset from 21 May to 22 Jun 2008.

d. Experiment setup

Three convective cases are investigated in this study. For each case, two different data assimilation experiments were carried out (CONV and SATCONV hereafter). Differences between CONV and SATCONV were only in the assimilated observational types. Only conventional observations were assimilated in CONV. The experiment SATCONV is the same as CONV except for adding *GOES-11* and *-12* radiance observations. Both the CONV and SATCONV experiments employed the same data assimilation system (GSI). The 6-h forecasts from NCEP Final Analysis (FNL) are used as the background fields ($\mathbf{x}_b$) at the beginning of the data assimilation cycle for initializing the data assimilation cycle of both the CONV and SATCONV experiments.

The conventional observations are composed of a global set of surface and upper-air reports operationally collected by NCEP, including land surface, marine surface, radiosonde and aircraft reports from the Global Telecommunications System (GTS), profiler and U.S. radar-derived winds, Special Sensor Microwave Imager (SSM/I) oceanic winds and atmospheric total column water (TCW) retrievals, and satellite wind data from NESDIS.

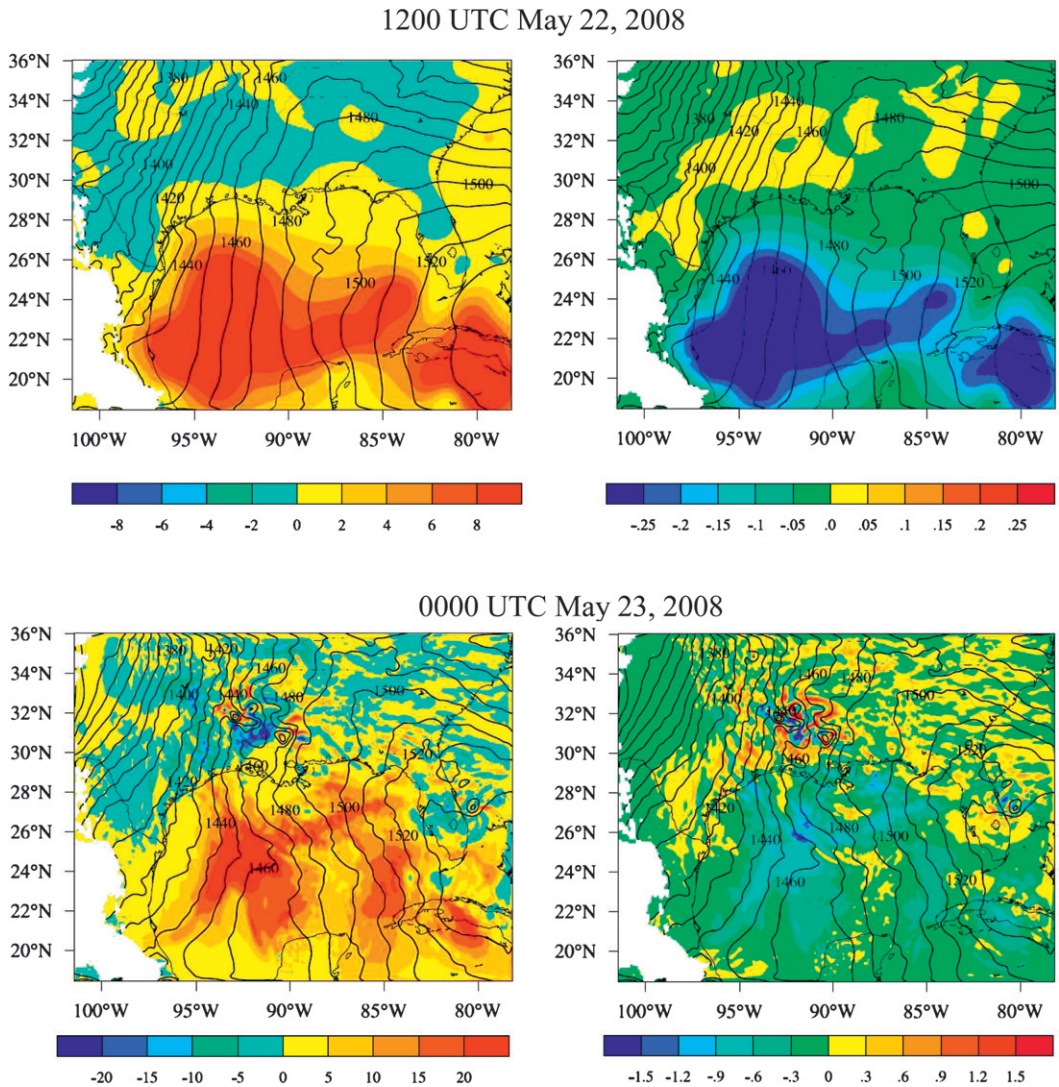

FIG. 5. Differences in (left) RH (shaded, %) and (right) temperature (shaded, °C) between SATCONV and CONV (SATCONV − CONV) and the geopotential of CONV (solid line, m) at 850 hPa at (top) 1200 UTC 22 May and (bottom) 0000 UTC May 23 2008.

For each case, four forecast experiments are carried out with four different sets of model initial conditions but the same model configuration. CTRL1 and CTRL2 are two model forecasts without data assimilation and they are initialized with NCEP FNL analyses at the beginning and end of the data assimilation cycle, respectively. Tables 1–3 provide a description of the three cases and the corresponding four numerical experiments conducted for each of the three cases. The version V3.0 of the Advanced Research core of the Weather Research and Forecasting (WRF) model (ARW) is selected as the forecast model. The horizontal resolution is 10 km. There are 27 vertical levels from the earth's surface to the model top specified at 50 hPa. The grid size of the model domain is 250 × 200 × 27. The WRF single-moment three-class microphysics scheme (Hong and Lim 2006), the Kain–Fritsch cumulus parameterization scheme (Kain and Fritsch 1990, 1993; Kain 2004), and the Yonsei planetary boundary layer scheme (Hong and Dudhia 2003) are selected for the ARW runs carried out in this study. The size of the model domain is shown later (Fig. 5).

3. GOES imagery data assimilation

GOES-11 or *-12* measures the reflected solar radiation and upwelling thermal infrared radiation from the surface and atmosphere. For infrared channels, the weighting function at a specified wavelength quantifies the

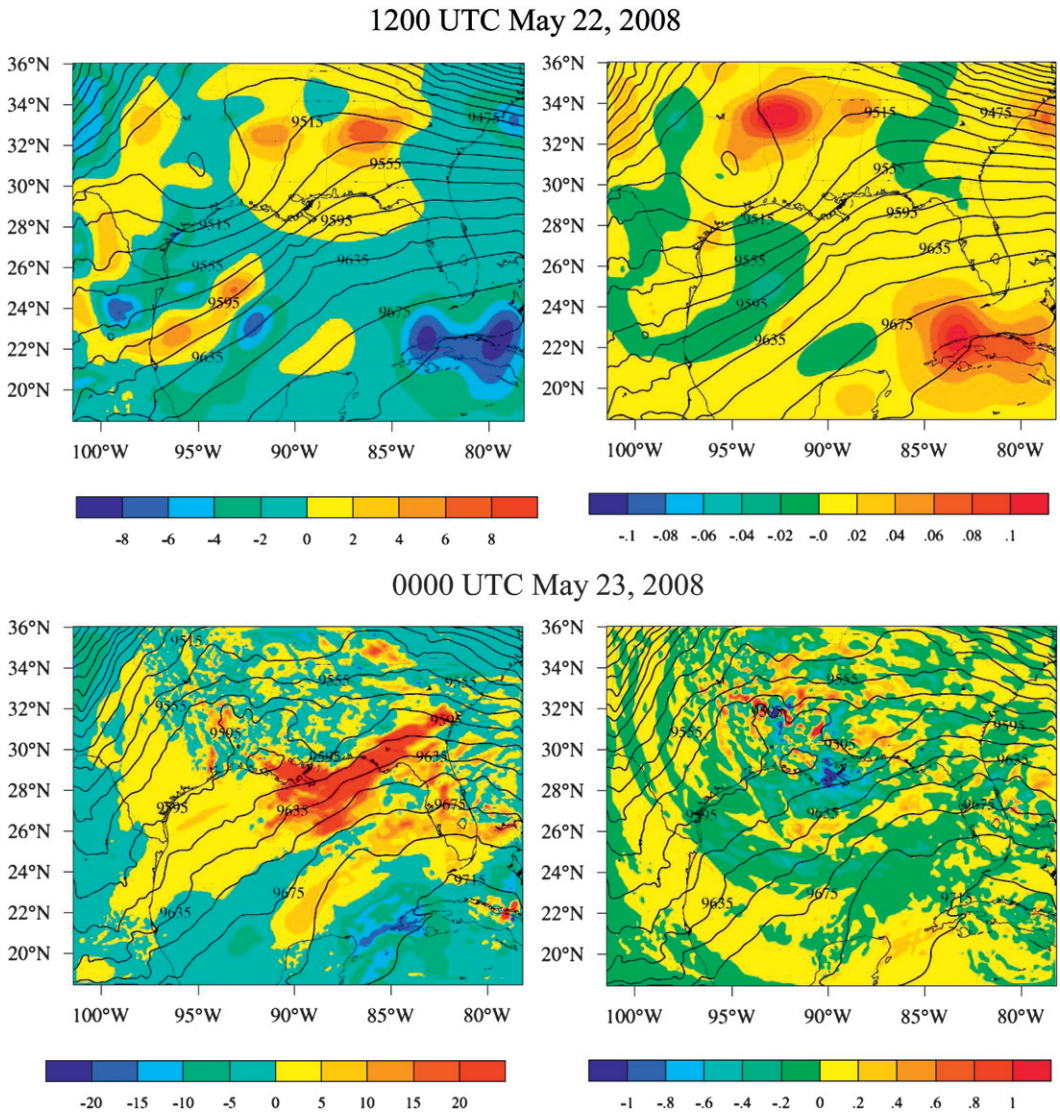

FIG. 6. As in Fig. 5, but at 300 hPa.

fraction of emitted radiation arising from various pressure levels. Therefore, weighting functions provide a general idea on the anticipated information content of different channels. The layer in which the weighting function peaks corresponds to the layer of the atmosphere to be most impacted by the assimilation of the corresponding channel. The weighting functions of the four imager channels from *GOES-11* and *-12* calculated from the *U.S. Standard Atmosphere, 1976* are displayed in Fig. 1. Also shown in Fig. 1 are the weighting functions generated using CRTM and averaged over approximately 200 and 400 cases during the 12-h data assimilation time window for *GOES-11* and *-12*, respectively. Compared with the weighting function profiles calculated from the *U.S. Standard Atmosphere, 1976* (solid lines in Fig. 1), these case-dependent profiles are in general broader than the standard profiles. The weighting functions of water vapor channel 3 of both *GOES-11* and *-12* peak on average around 400 hPa. Due to a slight difference in the central wavelength, the spectral response of water vapor channel 3 of *GOES-12* is broader than that of *GOES-11*. The weighting functions of *GOES-11* channel 5 and *GOES-12* channel 6 peak on average around 900 hPa. Channel 6 on *GOES-12* is located near the atmospheric CO_2 absorption band and is less sensitive to surface temperature than *GOES-11*'s channel 5. The GOES water-vapor radiances are composed mainly of information about moisture and temperature in the middle and upper troposphere, and the *GOES-12* CO_2 radiance consists of mainly information on the low-level temperature. The

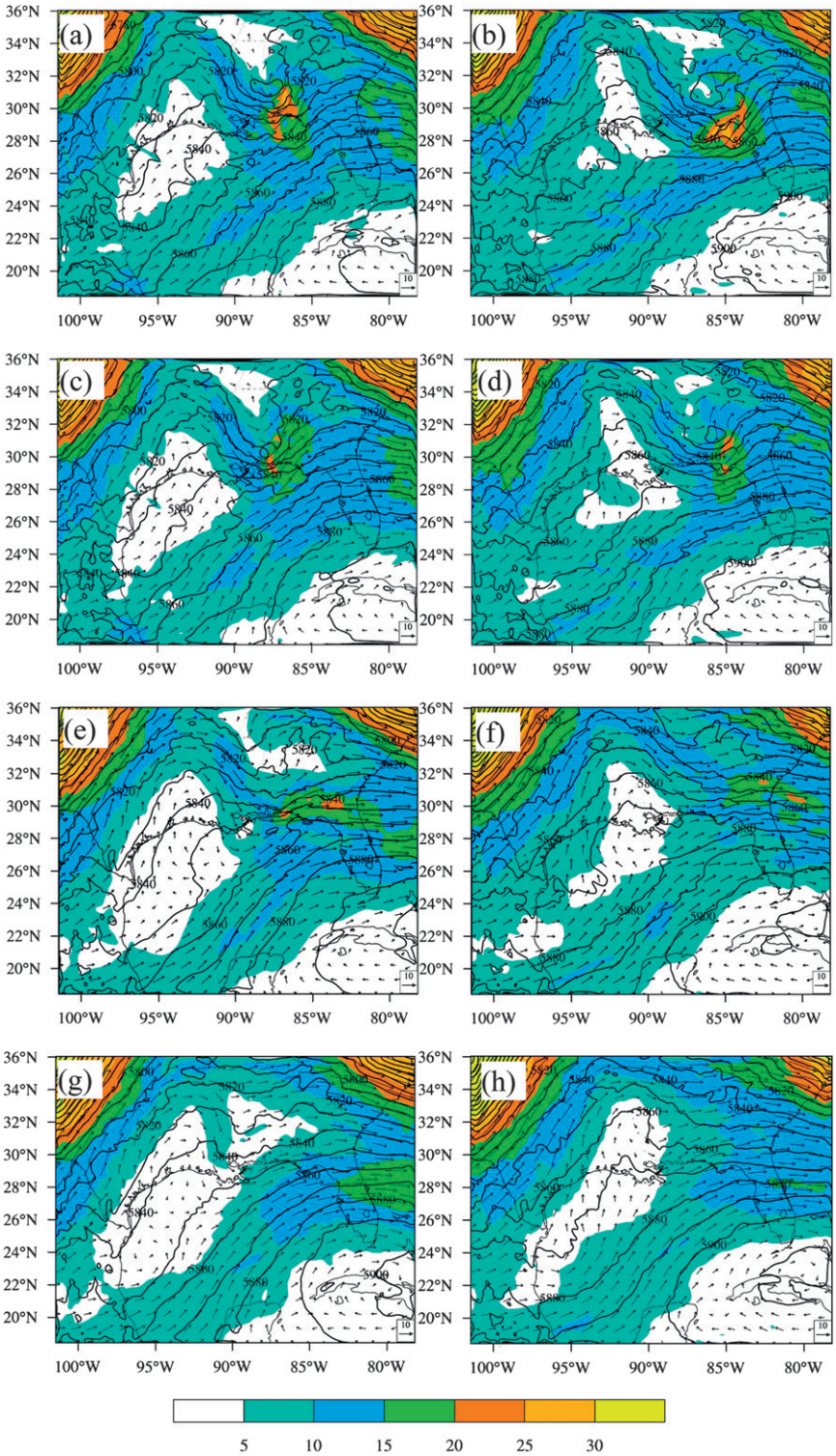

FIG. 7. The 500-hPa geopotential (solid line; contour interval is 10 m), wind vector, and wind speed (shaded, m s^{-1}) at (left) 1200 and (right) 1800 UTC 23 May 2008 from (a),(b) SATCONV; (c),(d) CONV; (e),(f) CTRL2; and (g),(h) CTRL1.

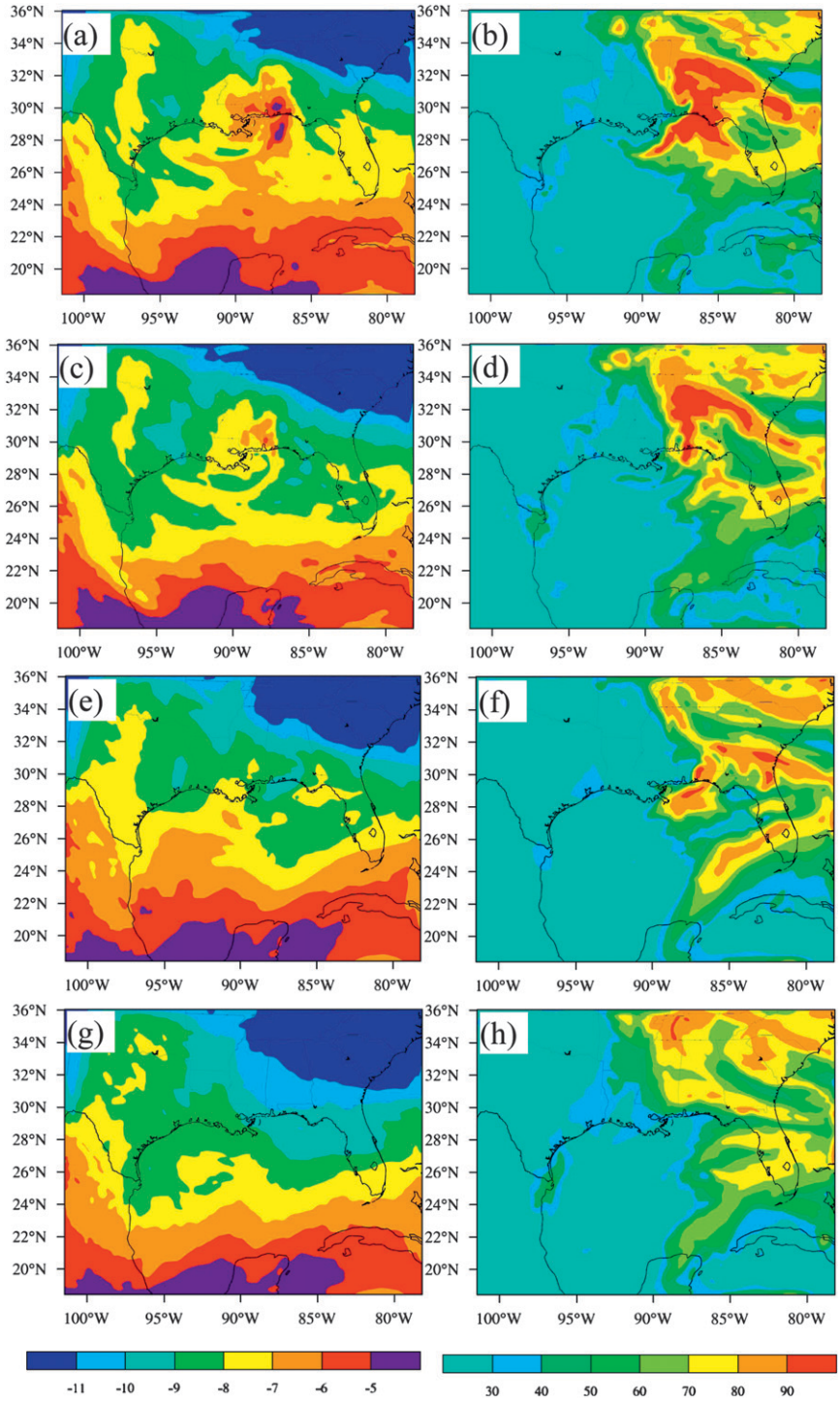

FIG. 8. The (left) 500-hPa temperature (shaded, °C) and (right) RH (shaded, %) at 1200 UTC 23 May 2008 from (a),(b) SATCONV; (c),(d) CONV; (e),(f) CTRL2; and (g),(h) CTRL1.

weighting functions of channels 2 and 4 peak at the surface. The radiances of channels 2, 4, and 5 are also strongly affected by surface emissivity. Channel 1 from both *GOES-11* and *-12* is not included in data assimilation since it is located at the solar wavelength and cannot be accurately simulated from the current forward model.

Spatial distributions of the *GOES-11* and *-12* brightness temperatures are shown in Figs. 2 and 3, respectively, at a

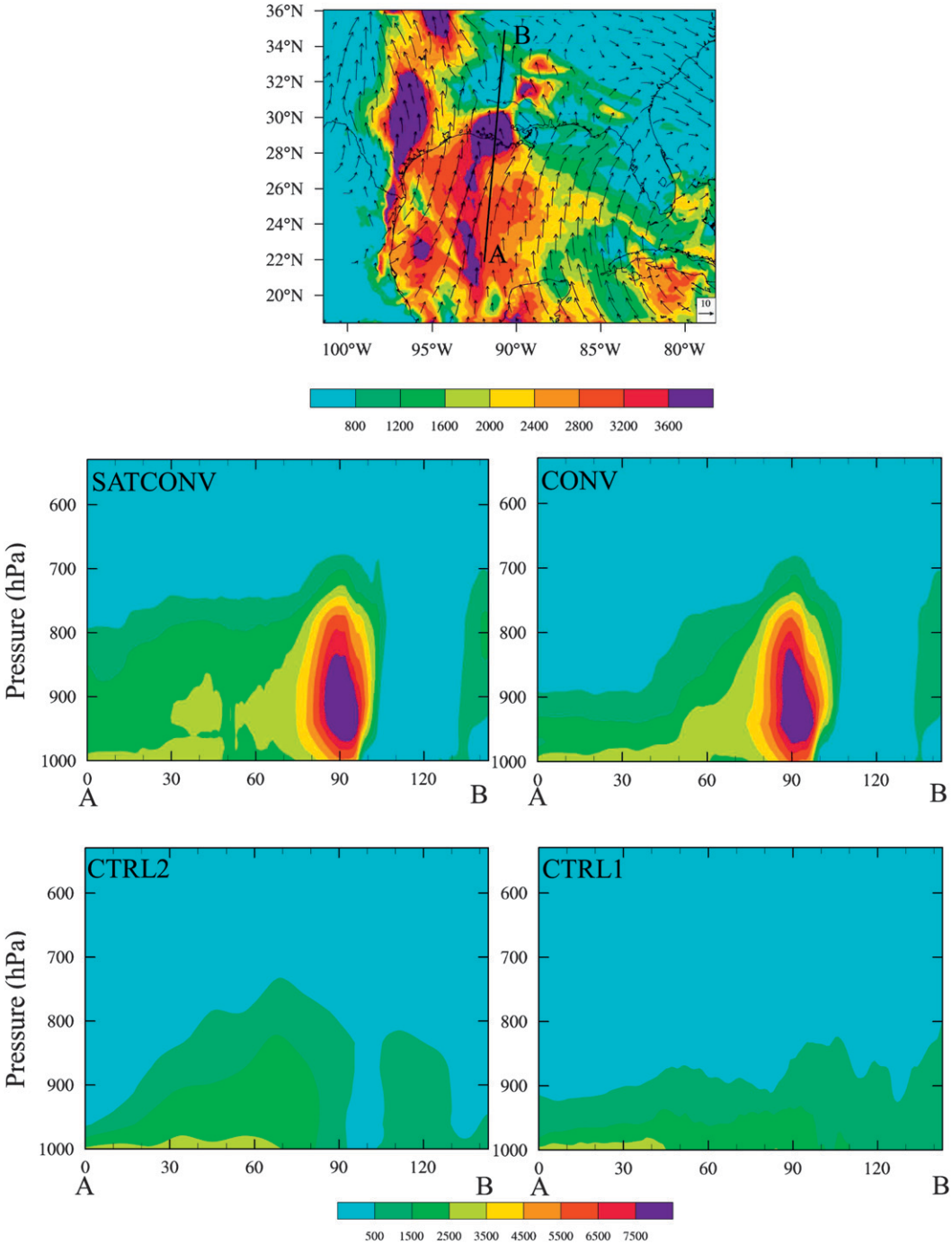

FIG. 9. (top) CAPE (J kg^{-1}) at 850 hPa from SATCONV at 0000 UTC 23 May 2008 and (bottom) cross sections of CAPE along the A–B line shown for SATCONV, CONV, CTRL2, and CTRL1.

single assimilation time: 1200 UTC 22 May. Observations removed from the assimilation by the GSI quality control procedure described in section 2c are indicated by open circles. It is seen that channels 2, 4, 5, and 6 are only used over ocean. Channel 3 results over both land and ocean are assimilated since it carries critical atmospheric water vapor information. *GOES-12* observations are used more than *GOES-11* observations, therefore providing a continuous stream rich in information over the ocean in the west and south of the Gulf of Mexico, where conventional data are sparse. Similar data distributions are seen at 1800 UTC 22 May and 0000 UTC 23 May 2008 (figures omitted).

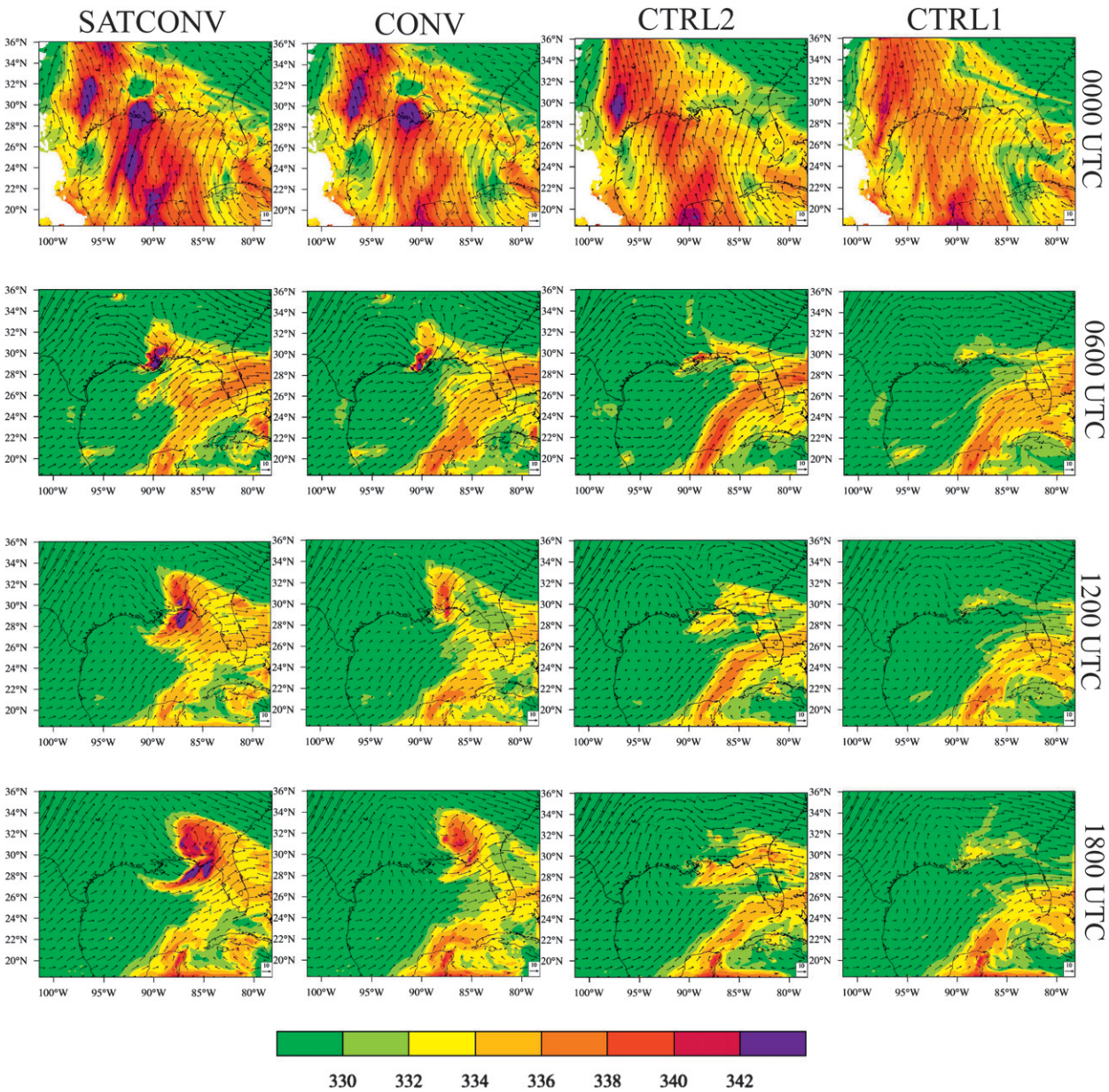

FIG. 10. (top) 850-hPa equivalent potential temperature (shaded, °C) and wind vector at 0000 UTC 23 May 2008; and 500-hPa equivalent potential temperature (shaded, °C) and wind vector at (second row) 0600 UTC, (third row) 1200 UTC, and (bottom) 1800 UTC 23 May 2008 from SATCONV (left), CONV (second column), CTRL2 (third column), and CTRL1 (right).

Mean biases were first calculated based on the error statistics of the innovations $[H(\mathbf{x}^b) - T_b^{\mathrm{obs}}]$, where $H(\mathbf{x}^b)$ represents the CRTM simulation using 1-month ARW 6-h forecast fields from 21 May to 22 June 2008, all initialized by NCEP FNL analyses. Positive biases are found in water vapor channels (1.09 and 1.59 K for *GOES-11* and *-12*, respectively) and small negative biases in other channels (−1.36, −0.78, and −0.63 K for *GOES-11* channels 2, 4, and 5, respectively; −1.09, −0.77, and −0.46 K for *GOES-12* channels 2, 4, and 6, respectively) during the investigated time period. A simple bias correction was applied during the GOES data assimilation by adding a fixed offset of the calculated mean bias to all the observations in a relevant channel. Biases and root-mean square (RMS) errors of *GOES-11* and *-12* observation departures from background and analysis for the SATCONV experiment are presented in Fig. 4, including 1 month of data from 21 May to 22 June 2008. Biases and RMS errors were reduced after the GOES data assimilation for all assimilated channels except for channel 2.

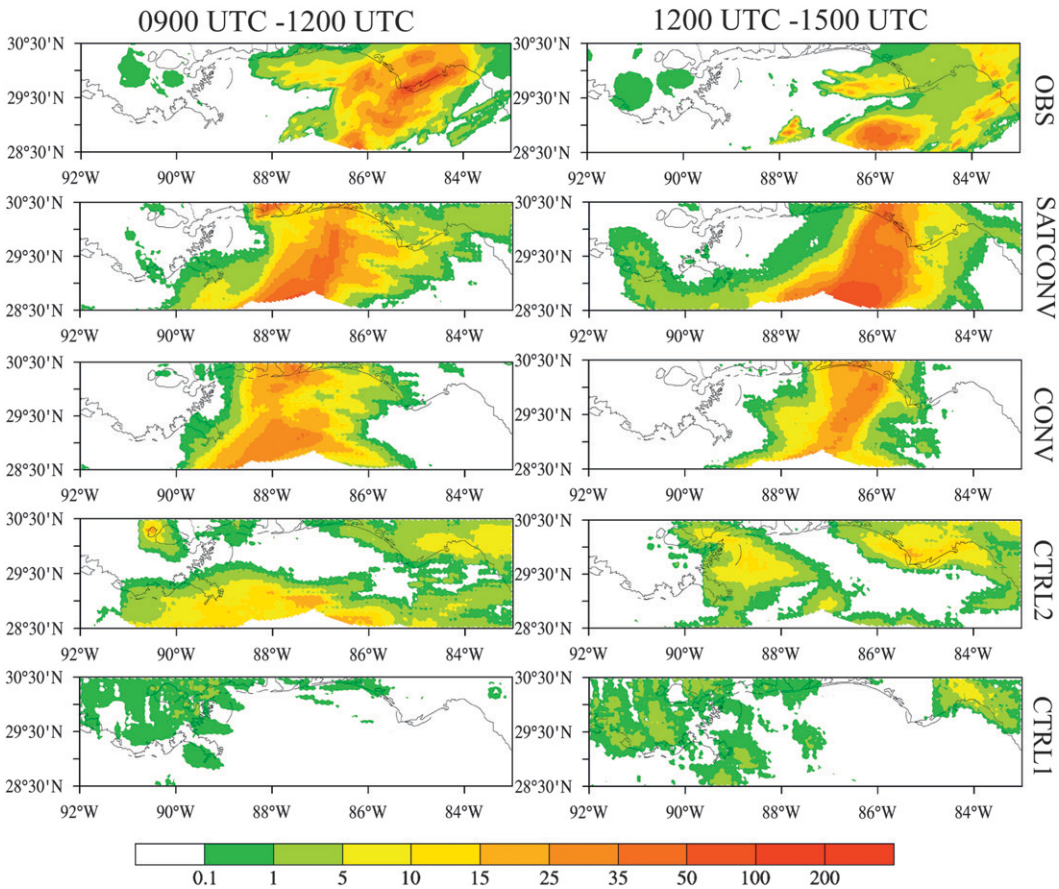

FIG. 11. The 3-h accumulative rainfall (mm) between (left) 0900 and 1200 UTC and (right) 1200 and 1500 UTC on 23 May 2008 near the coast of the Gulf of Mexico from (top) multisensor NCEP observations, (second row) SATCONV, (third row) CONV, (fourth row) CTRL2, and (bottom) CTRL1.

The most significant error reduction occurred at the water vapor channel for both *GOES-11* and *-12* at which the background error is the largest.

Differences in relative humidity and temperature analyses at 850 hPa between SATCONV and CONV at 1200 UTC 22 May and 0000 UTC 23 May 2008 are displayed in Fig. 5, along with the geopotential distribution from CONV at the same pressure level. It is noticed that over regions where *GOES-11* and *-12* data were assimilated (see Figs. 2 and 3), the relative humidity and temperature analyses become systematically wetter and colder. Since the 6-h forecast initialized with the analysis obtained by data assimilation at the previous analysis time was used as the background field, the GOES data impact propagates gradually into the northern Gulf of Mexico where no data are available. A 20% increase in relative humidity is seen along the two west branches of a split subtropical high, allowing more low-level water vapor advection into coastal areas. Figure 6 is similar to Fig. 5 except showing results from 300 hPa. At 1200 UTC 22 May, the differences in the relative humidity and temperature analyses at 300 hPa between SATCONV and CONV have an opposite sign compared to the low-level differences seen in Fig. 5 except for a streak of the atmosphere over the western Gulf of Mexico. Unlike in the low level, analysis differences between SATCONV and CONV are seen over land in the upper level. Due to larger wind, the GOES data impacts propagate faster into the northern Gulf of Mexico than in the low level. By 0000 UTC 23 May, a large area of 20% relative humidity difference appears near the Gulf coast, which favors the subsequent convective initiation.

4. Impacts on quantitative precipitation forecast

During the late spring and early summer, as the land heats up from daytime heating, an area of high pressure will form over the water and an area of low pressure over the land. The winds will shift around to the south, bringing a sea breeze with warm and moist air from the

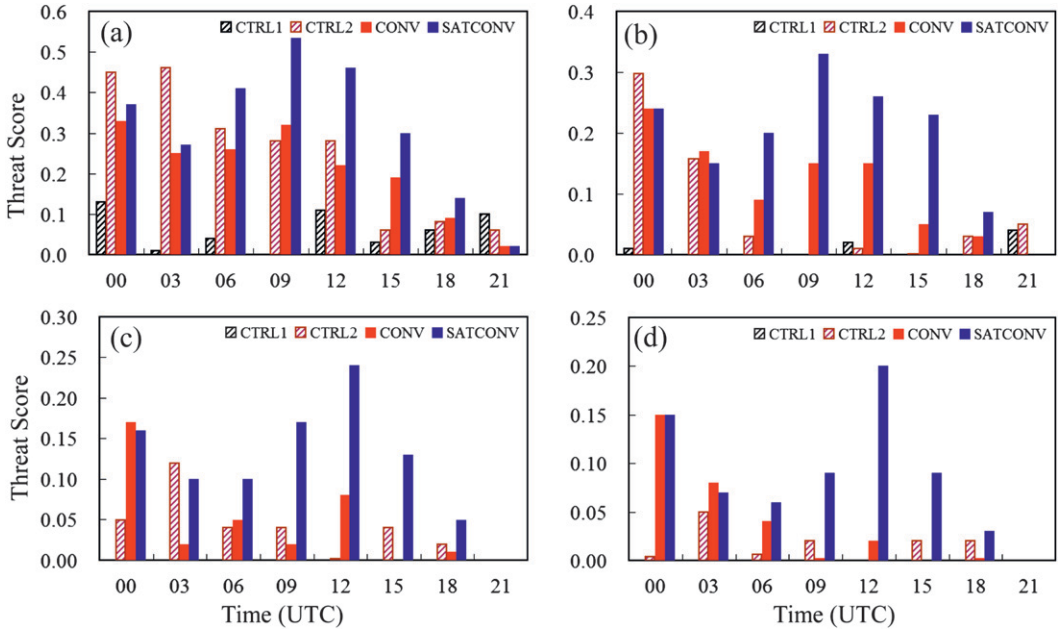

FIG. 12. Threat scores of 3-h accumulative rainfall from CTRL1, CTRL2, CONV, and SATCONV at (a) 1-, (b) 5-, (c) 10-, and (d) 15-mm thresholds from 0000 to 2400 UTC 23 May 2008.

Gulf of Mexico to the coastal regions. The warm moist air coming up from the Gulf of Mexico will collide with the cool dry air from the polar jet stream that moves from north to south, causing the development of thunderstorms. The thunderstorms can bring heavy rains to the coastal region of the Gulf of Mexico.

Prior to analyzing the impacts of GOES data assimilation on QPFs, a synoptic overview is first presented on the large-scale environment in which convection is initiated and developed. Figure 7 displays the 500-hPa geopotential and the wind vector and wind speed at 1200 and 1800 UTC 23 May 2008. A well-developed upper-level trough moved into the coastal area at 1200 UTC 23 May, and continued its further deepening while propagating farther to the southeast in SATCONV. The trough in CONV is slightly weaker at 1200 UTC and did not experience as much intensification or southeastward propagation as is seen in SATCONV. In contrast, the upper-level troughs in both CTRL1 and CTRL2 are significantly weaker than those of the two assimilation experiments (SATCONV and CONV) at 1200 UTC, and they weakened further at 1800 UTC 23 May 2008.

The temperature and relative humidity fields at 1200 UTC 23 May 2008 from SATCONV and CONV are shown in Fig. 8. Temperature in SATCONV is more than 2°C warmer than in CONV, CTRL1, and CTRL2 near the convective region. High relative humidity areas in CONV and CTRL1 are confined over land, while those in SATCONV and CTRL2 extend into the ocean and broader land area. Relative humidity in SATCONV is more than 20% wetter than CONV near the convective region and has a broader offshore area of high relative humidity than CTRL2.

A noticeable difference between SATCONV and CONV is found in the convective available potential energy (CAPE) distribution at 0000 UTC 23 May 2008. CAPE is a measure of the total maximum work the buoyancy force could do to an air parcel when the air parcel is lifted from the level of free convection to the level of neutral buoyancy. It is a good indicator of the severity a convective storm might attain. Figure 9 displays a spatial distribution and cross sections of CAPE in SATCONV, CONV, CTRL2, and CTRL1 at 0000 UTC 23 May 2008. It is seen that CAPE in SATCONV of more than 500 J kg^{-1} extends to as high as 700 hPa at the coast, with a long tail into the ocean. The CAPE layer in CONV is weaker and shallower than that of SATCONV over the ocean. There are nearly no strong convective features in either CTRL1 or CTRL2.

Before showing the impacts of GOES imager data assimilation on the 24-h prediction of the coastal precipitation forecasts, let us examine the outbreak of severe weather based on the equivalent potential temperature θ_e distribution. High θ_e indicates regions of warm and moist air where convection is more likely to occur. As shown in Fig. 10, a pocket of high-θ_e air is seen near the coast at 850 hPa in both SATCONV and CONV at 0000 UTC 23 May 2008. This air parcel reached 500 hPa at 0600 UTC, with SATCONV's θ_e

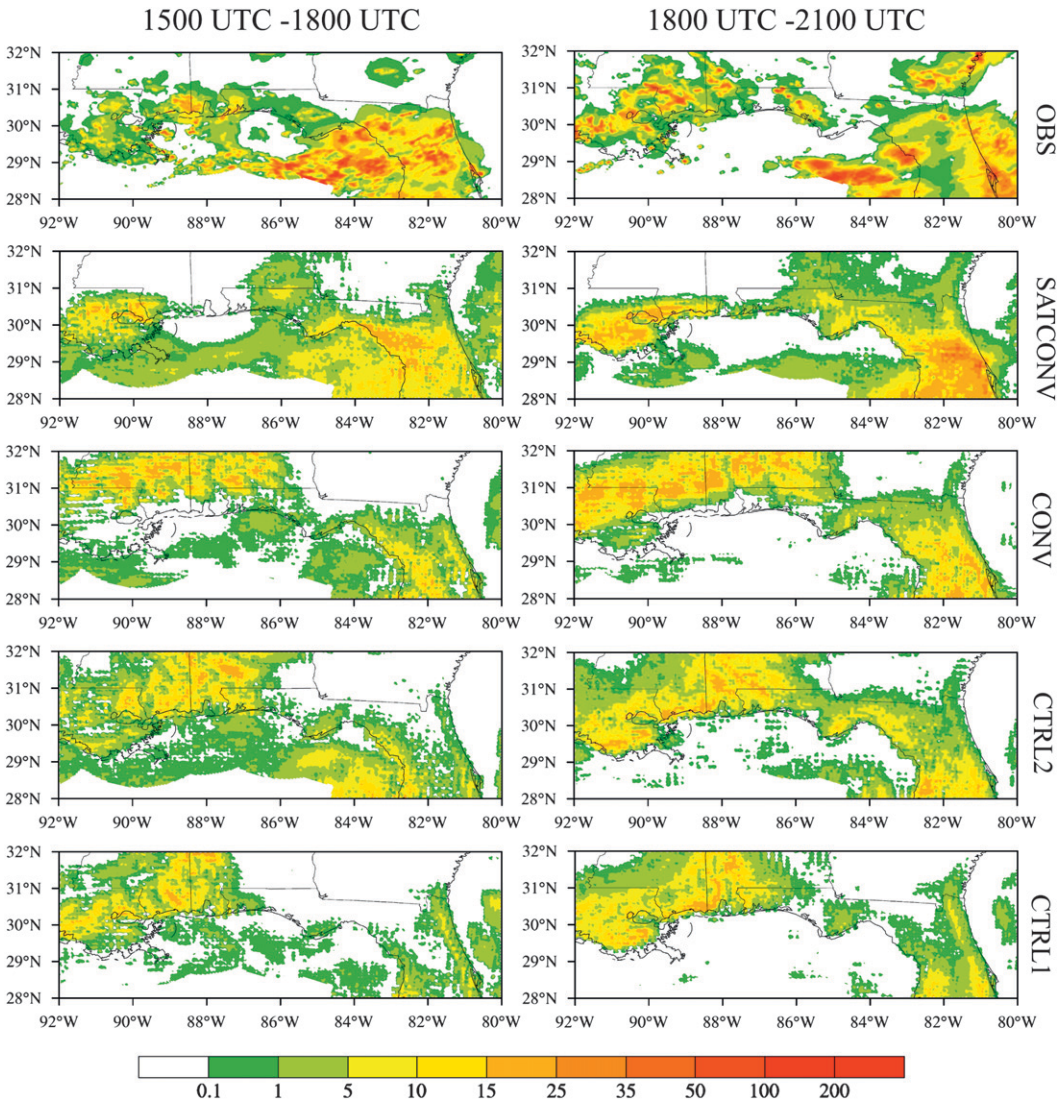

FIG. 13. The 3-h accumulative rainfall (mm) between (left) 1500 and 1800 UTC and (right) 1800 and 2100 UTC on 21 Jun 2008 (case two). All forecasts are initialized at 1800 UTC 20 Jun 2008.

being slightly larger than that of CONV. However, the high-θ_e air pocket in SATCONV moves southeastward and into the ocean while that in CONV stayed inland and weakened over time. A relatively high-θ_e air parcel off the coast is also seen in CTRL2, but it is weaker than that seen in SATCONV. In contract, a relatively high θ_e air pocket in CTRL1 is confined over land. The movement of the NCEP multisensor observed hourly precipitation (figure omitted) is similar to the temporal movement of the high-θ_e air pocket seen here in SATCONV.

Differences in the subsequent 24-h prediction of the coastal precipitation forecasts with and without the assimilation of *GOES-11* and *-12* imager radiances are presented in Figs. 11 and 12. Figure 11 presents the 3-h accumulative rainfall between 0900 and 1200 UTC and between 1200 and 1500 UTC (right panels) on 23 May 2008 near the coast of Gulf of Mexico from multisensor NCEP observations, SATCONV, CONV, CTRL2, and CTRL1. The GOES radiances assimilated were located over the nonrainy regions upstream of the coastal precipitation event (see Figs. 2 and 3). Their impacts start to show 6 h into the model forecasts. SATCONV performs better in capturing the observed eastward advancement of the precipitation event over time. However, both SATCONV and CONV overpredicted the precipitation over land. The CTRL2 performs best over land and CTRL1 fails to capture the eastward movement and development of the precipitation event.

Figure 12 displays the conventional threat scores of 3-h accumulative rainfall from CTRL1, CTRL2, CONV,

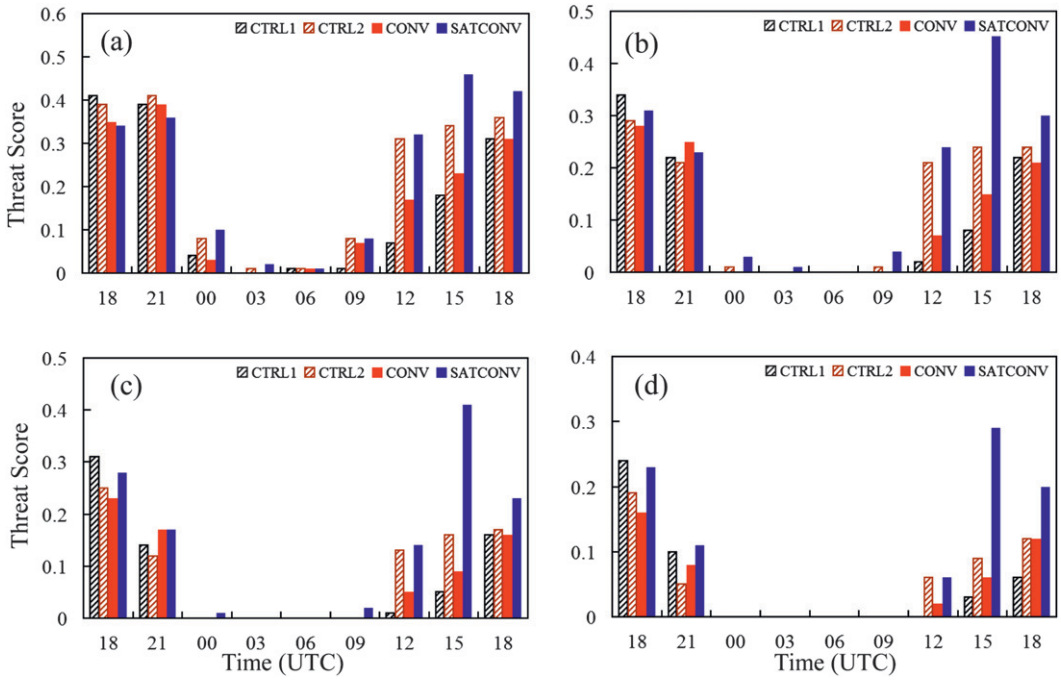

FIG. 14. Threat scores of 3-h accumulative rainfall from CTRL1, CTRL2, CONV, and SATCONV at (a) 1-, (b) 3-, (c) 5-, and (d) 7-mm thresholds from 1800 UTC 20 Jun to 2100 UTC 21 Jun 2008 (case two).

and SATCONV at different thresholds. Here, the threat score is defined as follows (Junker et al. 1992):

$$\mathrm{TS} = \frac{H}{F + O - H},$$

where F is the number of forecasts at the observation stations with precipitation equal to or exceeding a given threshold, O is the number of occurrences in which the observations meet or exceed the threshold, and H is the number of forecast "hits," where both the modeled and observed precipitation results meet or exceed the threshold. Thus, the conventional threat score indicates how accurately a precipitation threshold is predicted in a model forecast. It is pointed out that the bias-adjusted threat score, which indicates the likelihood of preserving or increasing the conventional threat score if forecasts are bias corrected based on past performance (Brill and Mesinger 2009), is not calculated because only discrete case studies are conducted here. From Fig. 12 it is seen that SATCONV outperforms all other forecast experiments at all thresholds after the 6-h model spinup time. The largest impact of GOES radiance assimilation is found for rainfall from 0600 to 1800 UTC, during which time convection was most active, and especially for heavier rain (larger thresholds). Compared with SATCONV, the forecast skill levels of the other three forecast experiments for light rain are higher than for heavier rain.

To further highlight the promise of GOES satellite imagery information observed in the preconvective environment for improved cloud and precipitation forecasts, two more case studies are carried out. During the 1-month period from 21 May to 22 June 2008, another two coastal precipitation events are found. One occurred from 1800 UTC 20 June to 2100 UTC 21 June 2008 (case two) and another from 1200 UTC 22 May to 0600 UTC 23 May 2008 (case three). The experiment designs for both cases are described in Tables 2 and 3, respectively. The impacts of GOES imager data assimilation on precipitation forecasts for both of these cases are shown in Figs. 13–16. The 3-h accumulative rainfall between 1500 and 1800 UTC (left panels) and that between 1800 and 2100 UTC (right panels) on 21 June 2008 from SATCONV, CONV, CTRL2, and CTRL1 for the second case are shown in Fig. 13. All forecasts are initialized at 1800 UTC 20 June. It is seen that all forecasts except for SATCONV overpredicted the precipitation over land. Both SATCONV and CTRL2 captured the precipitation pattern over the Gulf coast. Most improvements are seen 12 h into the model forecasts (Fig. 14) since there is nearly no precipitation during 0000–0900 UTC in the region shown in Fig. 3.

Improvements in coastal precipitation forecasts with direct assimilation of *GOES-11/12* imager radiances are also obtained in the third case (Table 3) based on the spatial distribution (Fig. 15) and threat scores (Fig. 16) of

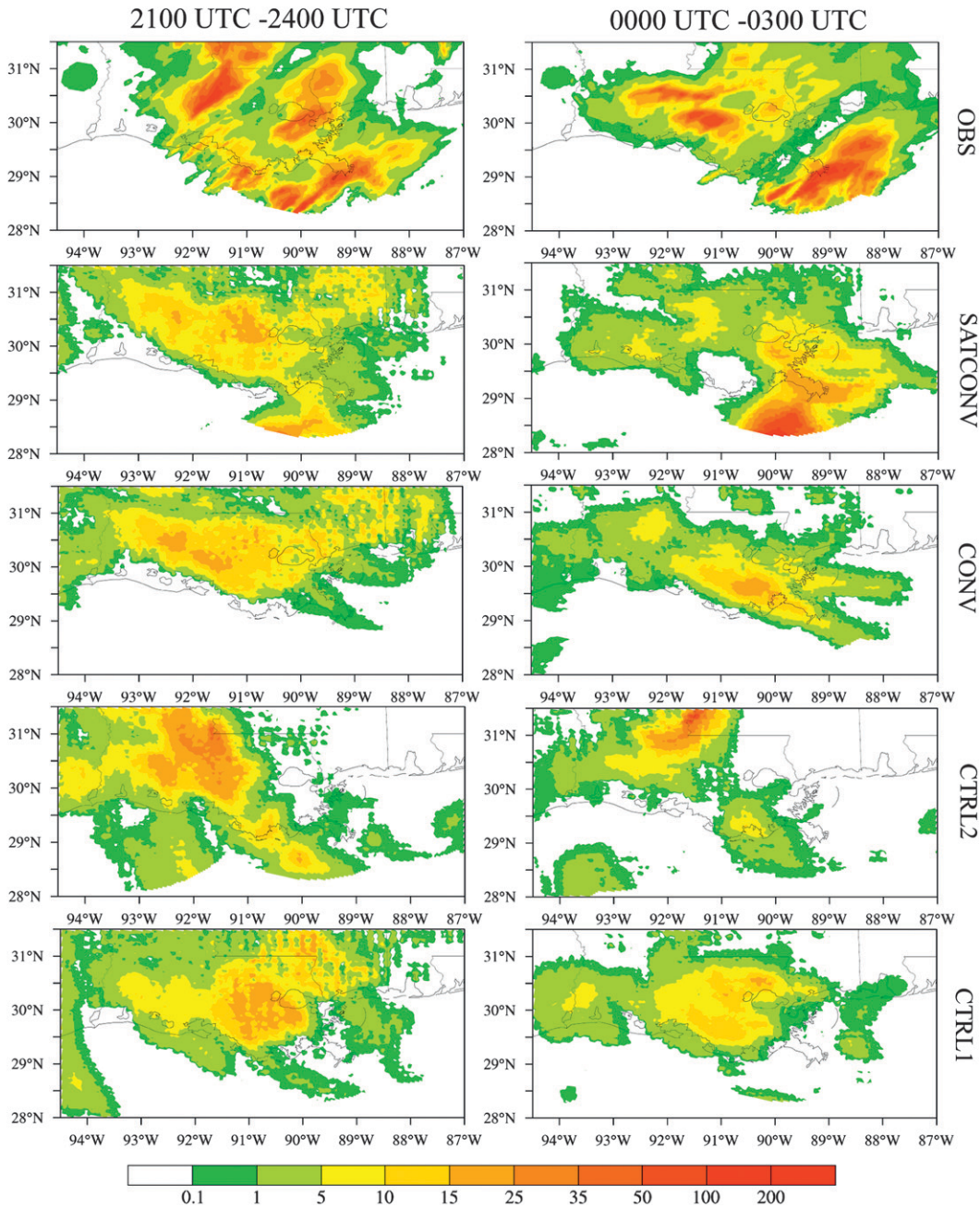

FIG. 15. The 3-h accumulative rainfall (mm) between (left) 2100 and 2400 UTC 22 May and (right) 0000 and 0300 UTC 23 May 2008. All forecasts are initialized at 1200 UTC 22 May 2008 (case three).

model-predicted precipitation. All experiments underpredicted the precipitation amount over land. However, the observed heavy precipitation off the East Coast is well captured only by SATCONV. Again, most of the improvement occurred after 9 h of model integration (Fig. 16) from a set of initial conditions in which GOES satellite imagery radiance observations in an upstream preconvective environment are incorporated into model initial conditions through a direct assimilation of GOES imagery radiance data.

5. Summary and conclusions

This paper examines the impacts of GOES IR radiances on analyses and forecasts of the limited-area ARW using the NCEP GSI analysis system. The channels

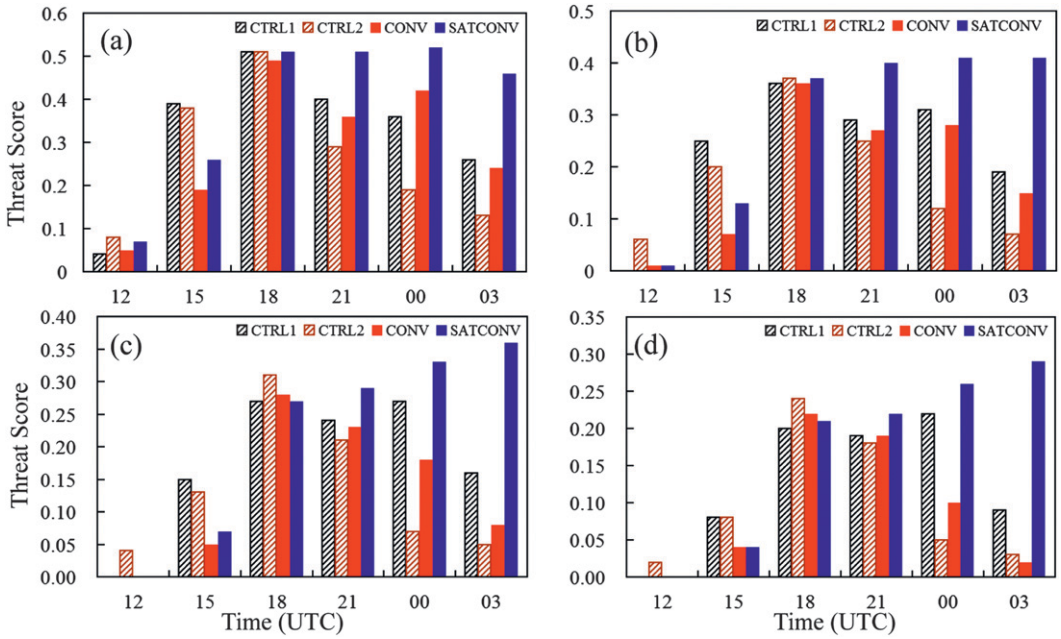

FIG. 16. Threat scores of 3-h accumulative rainfall from CTRL1, CTRL2, CONV, and SATCONV at (a) 1-, (b) 3-, (c) 5-, and (d) 7-mm thresholds from 1200 UTC 22 May to 0600 UTC 23 May 2008 (case three).

2–5 (3.9, 6.8, 10.7, and 12.0 μm) from *GOES-11* and channels 2–4 and 6 (3.9, 6.48, 10.7, and 13.3 μm) from *GOES-12* are used in the experiments. On land, only two water vapor channels (6.8 and 6.48 μm) were used since the rest of the IR channels are highly sensitive to the surface and cannot be simulated accurately at this time. Over oceans, all infrared channels were assimilated. Several data preparation steps were defined to conduct our quality control process. Two independent data assimilation experiments (CONV and SATCONV) were carried out to produce model initial conditions for each of the three coastal convective precipitation forecast cases using GOES data 6–12 h prior to convective initiation. The experiment CONV assimilated only conventional data and the experiment SATCONV made use of *GOES-11* and *-12* radiances under clear-sky or low cloud fraction conditions in addition to conventional observations.

A detailed analysis of a coastal precipitation event over the Gulf of Mexico is first conducted. Compared to CONV, the SATCONV analyses are in general wetter and colder to the west and south of the Gulf of Mexico where *GOES-11* and *-12* data were abundant. The largest differences were found in the middle troposphere. Such an analysis difference increased the offshore CAPE at 0000 UTC 23 May 2008, which is important for the subsequent development of convection. The GOES radiance assimilation also made a significant difference in the forecasting of an upstream trough that moved from northwest to southeast and modulated the movement of convective precipitation.

The evaluation of the ARW quantitative precipitation forecast accuracy against multisensor 3-hourly rainfall revealed very encouraging results for all three cases investigated in this study. The threat scores of the SATCONV precipitation forecast for all thresholds increased 6–9 h into the model forecasts when GOES data were assimilated. The present effort is different from assimilating precipitation observations to improve precipitation forecasts (e.g., Zou and Kuo 1996). Here, it is shown that GOES radiances over clear-sky conditions prior to convective initiation, when assimilated, had a significant positive impact on quantitative precipitation forecasts.

The preliminary results from this study highlight the potential benefits of assimilating GOES radiance observations for improved coastal precipitation forecasts. In the future, continuing effort will be made to (i) assess the impacts of GOES imagery brightness temperature measurements on regional NWP in the presence of other satellite radiance data currently assimilated in the operational system, (ii) use effectively the surface sensitive GOES IR channels as well as GOES radiances within cirrus clouds, and (iii) assimilate GOES imagery brightness temperature measurements at a data resolution much higher than the current resolution (40–60 km) for which issues related to observation error correlation

and modifications to background covariances have to be addressed.

Acknowledgments. This work was jointly supported by the Chinese Ministry of Science and Technology under Project 973, "Assessment, Assimilation, Recompilation and Applications of Fundamental and Thematic Climate Data Records" (2010CB951600), and NOAA's GOES-R Risk Reduction Program. The authors would like to express their sincere thanks to Dr. Tong Zhu and Mr. Greg Krasowski at the Joint Center for Satellite Data Assimilation (JCSDA) for their help in decoding GOES data and preparing GOES radiance BUFR data. The views and opinions contained in this paper reflects those of the authors and should not be construed as an official National Oceanic and Atmospheric Administration or U.S. government position, policy, or decision.

APPENDIX

GOES Imager Radiance Data Quality Control Procedure

Currently, GOES data are resampled, thinned, and converted to a new data format called the Binary Universal Form for the Representation of meteorological data (BUFR). The BUFR data contain the brightness temperature (TB), clear-sky fraction (clsky), and standard deviation (std) of the brightness temperature at 60- and 40-km resolution for *GOES-11* and *-12*, respectively. Here, std is the standard deviation of the raw data within the thinned 40- or 60-km box. An advantage with using coarse-resolution radiances is the reduction in observation error correlation. A new BUFR dataset at the original GOES resolution is being made for more advanced data assimilation experiments.

A multiple-step quality control (QC) procedure is applied to GOES imager radiance data before data assimilation. First, data with clsky less than 70% for *GOES-11* and *-12* are rejected. Data with a zenith angle greater than 60° are also rejected. Second, an empirical parameter a is calculated at each observation data point:

$$a = |r_i - r_k| \times \left[6.0\left(\frac{t_{\mathrm{obs}} - t_{\mathrm{ana}}}{60}\right) + \frac{10 - \mathrm{clsky}}{10} + 10 \times \mathrm{std} + \mathrm{sfc}\right].$$

The value of the parameter a depends on the temporal separation of an observation from the analysis time ($|t_{\mathrm{obs}} - t_{\mathrm{ana}}|$), the distance ($|r_i - r_k|$) of the observation location (r_k) from the center of the grid box in which the observation is located (r_i), the standard deviation (std) of the brightness temperature, and the surface type (sfc) at the data point. Here, the surface-type parameter, sfc, takes the following values: 0, 15, 10, 15, and 30 for sea, land, sea ice, snow, and mixed surface, respectively. The larger the values of $|t_{\mathrm{obs}} - t_{\mathrm{ana}}|$, $|r_i - r_k|$, std, and sfc are and the smaller the value of clsky is, the larger the value of the parameter a is. If the value of a from newly input data is greater than the previous one, the data are rejected at the second step. Otherwise, they are kept. The final QC step includes the following few checks: (i) negative brightness temperatures are removed; (ii) data from channels 2, 4, and 5 over land are rejected; (iii) all data over ice and snow surfaces are rejected; (iv) brightness temperature data are rejected if the standard deviation of brightness temperature, std, is greater than a prescribed value (see Table A1); and (v) brightness temperature data are rejected if they deviate from a background value by more than 3 times the observation error or the maximum error (see Table A1). Observation errors, which are required for GOES imager data assimilation, are also shown in Table A1 (NOAA/NESDIS 2010).

TABLE A1. Prescribed, observed, and maximum errors.

Channel	Prescribed std (K)	Observation error (K)	Max observation − background error (K)
2 (*GOES-11/12*)	1.0	2.0	4.5
3 (*GOES-11/12*)	1.5	1.4	4.5
4 (*GOES-11/12*)	1.0	3.0	4.5
5 (*GOES-11*)	1.0	3.0	4.5
6 (*GOES-12*)	1.0	3.0	4.5

REFERENCES

Andersson, E., J. Pailleux, J.-N. Thépaut, J. R. Eyre, A. P. McNally, G. A. Kelly, and P. Courtier, 1994: Use of cloud-cleared radiances in three/four-dimensional variational data assimilation. *Quart. J. Roy. Meteor. Soc.,* **120,** 627–653.

Brill, K., and F. Mesinger, 2009: Applying a general analytic method for assessing bias sensitivity to bias-adjusted threat and equitable threat scores. *Wea. Forecasting,* **24,** 1748–1754.

Derber, J. C., and W.-S. Wu, 1998: The use of TOVS cloud-cleared radiances in the NCEP SSI analysis system. *Mon. Wea. Rev.,* **126,** 2287–2299.

Eyre, J. R., G. Kelly, A. P. McNally, E. Andersson, and A. Persson, 1993: Assimilation of TOVS radiance information through one-dimensional variational analysis. *Quart. J. Roy. Meteor. Soc.,* **119,** 1427–1463.

Goerss, J. S., C. S. Velden, and J. D. Hawkins, 1998: The impact of multispectral *GOES-8* wind information on Atlantic tropical cyclone forecasts in 1995. Part II: NOGAPS forecasts. *Mon. Wea. Rev.,* **126,** 1219–1227.

Han, Y., F. Weng, Q. Liu, and P. van Delst, 2007: A fast radiative transfer model for SSMIS upper atmosphere sounding channels. *J. Geophys. Res.,* **112,** D11121, doi:10.1029/2006JD008208.

Hong, S. Y., and J. Dudhia, 2003: Testing of a new non-local boundary layer vertical diffusion scheme in numerical weather prediction applications. Preprints, *20th Conf. on Weather Analysis and Forecasting/16th Conf. on Numerical Weather Prediction,* Seattle, WA, Amer. Meteor. Soc., 20.3. [Available online at http://ams.confex.com/ams/pdfpapers/72744.pdf.]

——, and J.-O. J. Lim, 2006: The WRF single-moment 6-class microphysics scheme (WSM6). *J. Kor. Meteor. Soc.,* **42,** 129–151.

Junker, N. W., J. E. Hoke, B. E. Sullivan, K. F. Brill, and F. J. Hughes, 1992: Seasonal and geographic variations in quantitative precipitation prediction by NMC's nested-grid model and medium-range forecast model. *Wea. Forecasting,* **7,** 410–429.

Kain, J. S., 2004: The Kain–Fritsch convective parameterization: An update. *J. Appl. Meteor.,* **43,** 170–181.

——, and J. M. Fritsch, 1990: A one-dimensional entraining/detraining plume model and its application in convective parameterization. *J. Atmos. Sci.,* **47,** 2784–2802.

——, and ——, 1993: Convective parameterization for mesoscale models: The Kain–Fritsch scheme. *The Representation of Cumulus Convection in Numerical Models, Meteor. Monogr.,* No. 46, Amer. Meteor. Soc., 165–170.

Köpken, C., G. Kelly, and J.-N. Thépaut, 2004: Assimilation of Meteosat radiance data within the 4D-Var system at ECMWF: Assimilation experiments and forecast impact. *Quart. J. Roy. Meteor. Soc.,* **130,** 2277–2292.

McMillin, L., and H. Fleming, 1976: Atmospheric transmittance model of an absorbing gas: A computationally fast and accurate model for absorbing gases with constant mixing ratios in inhomogeneous atmospheres. *Appl. Opt.,* **15,** 358–363.

Nieman, S. J., J. Schmetz, and W. P. Menzel, 1993: A comparison of several techniques to assign heights to cloud tracers. *J. Appl. Meteor.,* **32,** 1559–1568.

NOAA/NESDIS, 2010: The GOES-14 Science Test: Imager and sounder radiance and product validations. NOAA Tech. Rep. NESDIS 131, 120 pp.

Purser, R. J., W.-S. Wu, D. F. Parrish, and N. M. Roberts, 2003a: Numerical aspects of the application of recursive filters to variational statistical analysis. Part I: Spatially homogeneous and isotropic Gaussian covariances. *Mon. Wea. Rev.,* **131,** 1524–1535.

——, ——, ——, and ——, 2003b: Numerical aspects of the application of recursive filters to variational statistical analysis. Part II: Spatially inhomogeneous and anisotropic general covariances. *Mon. Wea. Rev.,* **131,** 1536–1548.

Rao, P. A., C. S. Velden, and S. A. Braun, 2002: The vertical error characteristics of GOES-derived winds: Description and experiments with numerical weather prediction. *J. Appl. Meteor.,* **41,** 253–271.

Saunders, R. W., M. Matricardi, and P. Brunel, 1999: An improved fast radiative transfer model for assimilation of satellite radiance observations. *Quart. J. Roy. Meteor. Soc.,* **125,** 1407–1425.

Saunders, R., and Coauthors, 2007: A comparison of radiative transfer models for simulating Atmospheric Infrared Sounder (AIRS) radiance. *J. Geophys. Res.,* **112,** D01S90, doi:10.1029/2006JD007088.

Soden, B. J., C. S. Velden, and R. E. Tuleya, 2001: The impact of satellite winds on experimental GFDL hurricane model forecasts. *Mon. Wea. Rev.,* **129,** 835–852.

Stengel, M., P. Undén, M. Lindskog, P. Dahlgren, N. Gustafsson, and R. Bennartz, 2009: Assimilation of SEVIRI infrared radiances with HIRLAM 4D-Var. *Quart. J. Roy. Meteor. Soc.,* **135,** 2100–2109.

Su, X., J. Derber, J. Jung, Y. Tahara, D. Keyser, and R. Treadon, 2003: The usage of GOES imager clear-sky radiance in the NCEP global data assimilation system. Preprints, *12th Conf. on Satellite Meteorological and Oceanography,* Long Beach, CA, Amer. Meteor. Soc., 3.20. [Available online at http://ams.confex.com/ams/pdfpapers/56361.pdf.]

Szyndel, M. D. E., J.-N. Thépaut, and G. Kelly, 2005: Evaluation of potential benefit of SEVIRI water vapour radiance data from *Meteosat-8* into global numerical weather prediction analyses. *Atmos. Sci. Lett.,* **6,** 105–111.

Tomassini, M., G. Kelly, and R. Saunders, 1999: Use and impact of satellite atmospheric motion winds on ECMWF analyses and forecasts. *Mon. Wea. Rev.,* **127,** 971–986.

Velden, C. S., 1996: Winds derived from geostationary satellite moisture channel observations: Applications and impact on numerical weather prediction. *Meteor. Atmos. Phys.,* **60,** 37–46.

——, C. M. Hayden, S. J. Nieman, W. P. Menzel, S. Wazong, and J. S. Goerss, 1997: Upper-tropospheric winds derived from geostationary satellite water vapor observations. *Bull. Amer. Meteor. Soc.,* **78,** 173–195.

——, T. L. Olander, and S. Wazong, 1998: The impact of multispectral *GOES-8* wind information on Atlantic tropical cyclone track forecasts in 1995. Part I: Dataset methodology, description, and case analysis. *Mon. Wea. Rev.,* **126,** 1202–1218.

Weng, F., 2007: Advances in radiative transfer modeling in support of satellite data assimilation. *J. Atmos. Sci.,* **64,** 3799–3807.

Wu, W.-S., R. J. Purser, and D. F. Parrish, 2002: Three-dimensional variational analysis with spatially inhomogeneous covariances. *Mon. Wea. Rev.,* **130,** 2905–2916.

Zou, X., and Y.-H. Kuo, 1996: Rainfall assimilation through an optimal control of initial and boundary conditions in a limited-area mesoscale model. *Mon. Wea. Rev.,* **124,** 2859–2882.